Rate-Energy Tradeoff Analysis in RIS-SWIPT Systems With Hardware Impairments and Phase-Based Amplitude Response

WAQAS KHALID[1], **HEEJUNG YU**[2], **(Senior Member, IEEE), JUPHIL CHO**[3], **ZEESHAN KALEEM**[4], **(Senior Member, IEEE), AND SHABIR AHMAD**[5], **(Member, IEEE)**

[1]Institute of Industrial Technology, Korea University, Sejong 30019, South Korea
[2]Department of Electronics and Information Engineering, Korea University, Sejong 30019, South Korea
[3]Department of Integrated IT and Communication Engineering, Kunsan National University, Kunsan 54150, South Korea
[4]Department of Electrical and Computer Engineering, COMSATS University Islamabad, Wah Campus, Wah Cantt 47040, Pakistan
[5]Department of IT Convergence Engineering, Gachon University, Seongnam-si 461-701, South Korea

Corresponding authors: Heejung Yu (heejungyu@korea.ac.kr) and Juphil Cho (stefano@kunsan.ac.kr)

ABSTRACT This paper investigates the reconfigurable intelligent surface (RIS)-empowered dynamic power splitting designs for simultaneous wireless information and power transfer (SWIPT) systems while adopting various practical hardware issues. Specifically, we adopt the physical size of the RIS and the placement of the RIS plane to phase-align the reflected signals towards the desired direction. The analytical phase shift model for the reflecting elements is presented to characterize an intertwined relationship between amplitude and phase responses, which captures the amplitude variations depending on phase in RIS elements. Furthermore, an additive distortion noise incorporates the residual transceiver hardware impairments (RTHIs). The stringent signal-to-interference-plus-noise ratio requirement is facilitated using both the direct and indirect, i.e., RIS cascaded, links. To made complicated analysis become tractable, we exploit the statistical properties of the effective channel power which follows a Gamma distribution. The tight bounds for the achievable rates and residual energy are derived and the tradeoffs between the achievable rate and residual energy for the time switching and static power splitting designs are characterized. Finally, the numerical results confirm the accuracy of the developed framework and demonstrate the selection of the system parameters.

INDEX TERMS RIS, SWIPT, RTHIs, phase-dependent amplitude response, rate-residual energy tradeoffs.

I. INTRODUCTION

The deployment and standardization activities of fifth generation (5G) wireless networks are rapidly increasing. 5G networks enable various functional requirements, such as ultra reliability, sub-millisecond end-to-end latency, multi-Gbps peak data speeds, high connectivity/optimization for Internet-of-Things (IoTs), ultra capacity and order-of-magnitude improvements in the link robustness, energy efficiency and spectrum allocation flexibility/utilization efficiency [1], [2]. The key enabling technologies of 5G networks include multiple-input multiple-output (MIMO) [3], non-orthogonal multiple access (NOMA) [4], ultra-dense small cells deployment [5], millimeter wave (mmWave) bands [6], and

The associate editor coordinating the review of this manuscript and approving it for publication was Cong Pu.

cognitive radio (CR) networks [7], [8]. Despite these revolutionary technologies, 5G cannot meet all the requirements. Triggered by this, the conceptualization of the sixth generation (6G) networks has begun to sustain the competitive edge of wireless communications.

The active research campaigns has been started for future 6G networks and the standard and trials will be completed by 2028 [9]. The core requirements, service categories and enabling technologies promise a revolutionary future with 6G networks. The technological advantages and disruptive capabilities will provide the innovative use-cases, data-intensive applications, unprecedented services, excellent quality-of-service (QoS), ubiquitous intelligent connectivity and encompassing solutions for the 2030 and beyond. To this end, the potential key enabling technologies and solutions of future 6G networks include massive

MIMO [10], dynamic spectrum sharing with full-duplex (FD)/device-to-device (D2D) communications [11], artificial intelligence (AI) [12], terahertz (THz) bands [13], nonterrestrial communications [14], reconfigurable intelligent surface (RIS) [15], and simultaneous wireless information and power transfer (SWIPT) [16]. In particular, RIS and SWIPT are the novel technologies to enable the energy efficiency and spectrum efficiency and provide the innovative solutions to the inherent challenges in the developments of the 6G systems.

In detail, an RIS is a promising cost-effective physical-layer technology to achieve the higher spectral and energy efficiency, and thereby have gained a lot of attention from the wireless communication industry [17]. RISs smartly modify the wireless propagation channels, i.e., realize the controllable and programmable radio environment, and thereby mitigate a wide range of challenges in non-line-of-sight (NLoS) scenarios. RISs provide supplementary links to assist the transmissions, thereby improving both the QoS and radio connectivity. A typical RIS with a large number of passive reflecting elements reflects the incoming signals independently with the controllable phase shifts. The fine-grained reflect beamforming (via controlling the phases and/or amplitudes induced by the reflecting elements) can be designed to perform the advanced wireless functions, e.g., signal enhancement or suppression. The RIS can overcome the unfavorable radio-frequency (RF) propagation conditions, such as blockage and deep fading, through intelligent placement and reflect beamforming designs. Furthermore, the joint active and passive beamforming design, i.e., by modifying the RF propagation along with optimized signal processing at the transceiver, brings extraordinary benefits for the 6G wireless paradigm, including coverage and throughput enhancements (via signal boosting and reliable reception), interference cancelation, secure communications (via physical layer security), and information and power transfer, etc. [18]. The other undeniable performance advantages of an RIS include agile deployment, real-time configuration, full-duplex transmission, low complexity hardware architecture, limited control messages, and superior transmission and passive relay performances.

As a parallel trend, the integration of wireless power transfer with communication networks has led to the novel SWIPT technology which also has drawn an upsurge of research interest [19]. SWIPT is an effective technology to transfer both the information and power to end-devices simultaneously via RF signals and ease the contradiction between the high transmission rate and long lifetime of battery-powered devices. SWIPT is an innovative candidate and a promising green communication solution for the energy-constrained communication networks as well as IoT applications. The implementation of SWIPT techniques with communication technologies, including MIMO, NOMA, heterogeneous CR networks and FD/D2D/mmWave communications, etc., is a novel design approach in 5G/future 6G networks. The effective incorporation of SWIPT techniques in 5G/future 6G scenarios achieves the substantial performance gains in terms of energy consumption, spectral efficiency, interference management and transmission delays, but also brings several challenges that need to be addressed [20].

A. RELATED WORK

The aforementioned works related to SWIPT technology have extensively covered both the technical and theoretical perspectives. The research contributions were extended in terms of the communication protocols, circuit designs and signal processing and wireless networking. The other related topics were also covered, including basic concepts, use case scenarios, recent developments, technical challenges and future directions [21]. In a nutshell of the prior research, the effective SWIPT receiver architecture has been recognized as a challenging problem. A proper information and power design was crucial for the noteworthy energy-efficient and reliable wireless communications. On the other hand, the challenges related to the RIS-deployment, including channel estimation, robust design with imperfect channel parameters, security and privacy, passive information transfer, mobility management, placement and configuration, hardware limitation (e.g., phase quantization errors and number of reflecting elements) and AI/ML-enabled design and optimization for the passive beamforming, have been explored [22], [23].

In further developments, RISs have been combined with SWIPT to drastically improve the spectral efficiency and energy efficiency for 5G/future 6G networks [24]. In general, the performance in terms of reception reliability can be evaluated by the achievable information rates. The practically realizable SWIPT receivers could only be obtained in the domains of power, time, antenna and space, using the approaches, including power splitting, time switching, antenna switching and spatial switching, respectively. This was because that the circuit technology limited the concurrent energy harvesting (EH) and information decoding (ID) operations on the same received signal. In this respect, the tradeoff between the information rate and harvested energy, also called the rate-energy (R-E) tradeoff, identified the amount of information transfer and the amount of energy transfer and conventionally evaluated the system performance. The R-E tradeoff was determined by the appropriate resource management, i.e., information and energy allocation, and was essential and crucial for characterizing and understanding the fundamental performance of RIS-aided SWIPT systems [25]. In the closely related prior research, the optimization of the transmit beamforming as well as reflective beamforming was suggested to minimize the transmit power or to maximize the sum rate/or sum-power of the information/or energy receiver under certain harvested energy/or information rate constraint at the energy/or information receiver [26].

B. MOTIVATION, NOVELTY AND CONTRIBUTION

Despite the extensive and individual studies, the development of RIS-aided SWIPT systems in 5G/future 6G networks while adopting various practical issues remains to

be tackled. For example, the prior works assumed the ideal phase shift model for the RIS with the maximum signal reflection for the reflecting elements, i.e., the amplitude response was constant and independent of the induced phase shift. Such an ideal reflection control could only be obtained when the reflecting elements exhibited the zero energy dissipation. However, the energy dissipation is unavoidable and is a long standing problem for the reflection-based metasurfaces [27]. Therefore, the phase shift model with the intertwined relationship between the reflection amplitude and phase shift responses due to practical circuit implementation of the reflecting elements must be incorporated. Besides, the sum of the power consumptions at the transmitter and the SWIPT receiver, in practice, can accurately model the total power consumption of the link [28]. The power consumption can be engaged in energy conversion efficiency for the SWIPT energy receiver and otherwise, can be considered negligible due to the passive devices. However, the SWIPT information receiver requires the non-negligible circuit power. It is important to consider the receiver circuit power consumption for the low-power applications (e.g., wireless sensor networks) where energy-efficient transmission is needed. In this correspondence, the achievable rate-residual energy (R-Er) tradeoff (i.e., by employing the residual energy as the harvested energy minus the consumed energy) provides a more general framework for RIS-aided SWIPT systems.

Furthermore, the fading channel plays a vital role in the performance analysis. While employing RIS-aided SWIPT systems, the existing Literature, in general, focused the Rayleigh and Nakagami-m distributions for the small-scale fading and the link distance for the large-scale fading. Similar to a phased array, a RIS achieves the coherent beamforming in a desired direction via phase shifting of its reflecting elements. However, the path loss expression must be derived and the phase-shifts must be explicitly optimized when the superposition of multiple signals (via RIS-cascaded and LoS links) are considered. Furthermore, the placement of the RIS plane and the physical features of the RIS are the significant yet traditionally neglected considerations for the path loss expression and accurately modeling the RIS-aided communications [29]. Finally, the impact of inevitable RF front-end related impairments must be considered to facilitate the practical nature of the wireless transceiver hardware equipment. To this end, the aggregate impairment has a non-negligible deleterious impact on the system performance owing to the fundamental capacity ceiling which cannot be eliminated by simply increasing the transmit power. In this respect, the compensation algorithms at the receiver and calibration techniques at the transmitter can be used. However, the full elimination is not possible [30]. The remaining unaccounted distortion was generally referred as the residual transceiver hardware impairments (RTHIs). The RTHIs can be efficiently modeled as the additive Gaussian noise to have the analytical tractability and the experimental verification.

The aforementioned works have considered the above mentioned practical issues in simpler setups only. To the best of our knowledge, the ideal conditions were considered when turning the focus into the complicated analyses, and the related studies resorted to the simplified models to reduce the consequent design complexity. The RIS-aided SWIPT systems result in a complicated mathematical description when are employed with the non-ideal parameters. The prior works does not focus on the above-mentioned issues and bridging these gaps is the motivation behind our work. The technical contribution of this paper is summarized as follow:

- *System settings*: We present a novel theoretical framework for RIS-aided SWIPT systems to investigate the R-Er tradeoffs for the time switching (TS) and static power splitting (SPS) designs. Specifically, we consider the phase-dependent amplitude variations in element-wise reflection coefficient for the RIS. This paper also grapples with the thorough investigation of residual additive transceiver impairments. In addition, a rigorous path loss model builds the system model for the RIS-aided communications and characterizes the received signal power as a function of the area of the RIS and the rotation of the RIS plane.
- *Performance analysis*: We provide the statistical characterization for the tractable analysis. The Gamma distribution is utilized for the approximation of the effective channel power gain and the related statistics are derived. The tight bounds of the performance metrics, i.e., achievable rate and residual energy, are derived and the R-Er tradeoffs for the TS and SPS designs are quantified in novel analytical expressions.
- *Insightful observations*: The results confirm the accuracy and effectiveness of the analytical framework and demonstrate the selection of the system parameters for the TS/SPS designs, including the area of the RIS, placement of the RIS plane, physical size and number of the reflecting elements and constants related to the RTHI and the practical phase shifters. As a fringe benefit, this paper provides the design insights for the RIS-aided SWIPT systems.

C. NOTATIONS AND PAPER ORGANIZATION
1) NOTATION
In this paper, the symbol $\dot{\sim}$ stands for approximately following an distribution, $|.|$ the absolute value and $\mathbb{E}\{X\}$, $\mathbb{V}\{X\}$, $f_X(.)$ and $F_X(.)$ the statistical expectation, variance, probability density function (PDF) and cumulative distribution function (CDF) of a random variable ($\mathcal{RV}$) X, respectively. $\log(.)$ and $\ln(.)$ stand for the binary and natural logarithm functions, respectively, $K_v(.)$ stands for the modified Bessel function of the second kind and the Gamma function is defined by the Euler integral as $\Gamma(s) = \int_0^\infty t^{s-1}e^{-t}dt$. Furthermore, $\mathcal{CN}(t_1, t_2)$ represents the complex Gaussian distribution with mean value t_1 and variance t_2.

TABLE 1. List of abbreviations.

Abbreviation	Description
RIS	Reconfigurable intelligent surface
R-Er	Achievable rate-residual energy
SWIPT	Simultaneous wireless information and power transfer
5G	Fifth generation
IoT	Internet-of-Things
MIMO	Multiple-input multiple-output
NOMA	Non-orthogonal multiple access
mmWave	Millimeter wave
CR	Cognitive radio
6G	Sixth generation
QoS	Quality-of-service
FD	Full-duplex
D2D	Device-to-device
THz	Terahertz
LoS	Line-of-sight
RF	Radio frequency
EH	Energy harvesting
ID	Information decoding
RTHIs	Residual transceiver hardware impairments
TS	Time switching
SPS	Static power splitting
SINR	Signal-to-interference-plus-noise ratio

TABLE 2. List of notations.

Notation	Description
M	Number of reflecting elements in an RIS
L_{RIS}	Pathloss of an indirect path
L_0	Pathloss of a direct path
θ_i	Incident angle
θ_{Rot}	Rotation angle of an RIS plane
θ_R	Target angle
$X_R (Y_R)$	Aggregate length (width) of the M reflecting elements
l	Side length of the square reflecting element
$f_a(\theta_f)$	Amplitude (Phase) of the channel f
$\alpha_m(\theta_m)$	Amplitude (Phase) of the channel h_m
$\kappa_m(\epsilon_m)$	Amplitude (Phase) of the channel g_m
χ_m	Reflection coefficient for the mth element
$\psi_m(\phi_m)$	Amplitude (Phase) for the mth element
ψ_{min}	Minimum amplitude for practical phase shifters
ϑ, ϖ	Constants related to practical phase shifters
$\omega_S (\omega_D)$	Distortion noise due to residual impairment at S (at D)
$\zeta_S (\zeta_D)$	Constant controlling the residual impairment at S (at D)
ω_T	Aggregate distortion noise due to RTHIs
ζ_T	Constant controlling the RTHIs
x_T	Signal intended for D
K	Number of transmitted symbols per block
t_s	Symbol period
η	Energy conversion efficiency
β	Power splitting ratio
α	Time switching ratio
P_C	Circuit power consumption at D
ρ_S	Ratio between transmit power and noise power
$E_R{}^{TS}$	Residual energy for the TS design
$E_R{}^{SPS}$	Residual energy for the SPS design
$R_A{}^{TS}$	Achievable rates for the TS design
$R_A{}^{SPS}$	Achievable rates for the SPS design

2) PAPER ORGANIZATION

The reminder is organized as follows. Section II provides the system model, including the network description, channel modeling and phase shift and signal transmission models. Section III presents the analytical framework of the TS and SPS designs and the statistical characterization of the R-Er tradeoffs for the performance analysis. In Section IV, we discuss the extension to RIS correlated channels and nonlinear EH model. Section V reports the numerical results and discussion. Finally, we conclude the paper in Section VI.

The abbreviations and notations used in this paper are listed in Tables 1 and 2, respectively.

II. SYSTEM MODEL
A. NETWORK DESCRIPTION

As shown in Fig. 1, we consider the point-to-point downlink transmissions for RIS-aided SWIPT systems. A single-antenna base station (S) communicates with a single-antenna SWIPT user (D) where D is enabled with the dynamic power splitting operations, e.g., TS and SPS. An RIS is deployed to assist the transmissions of S.[1] Specifically, the phase shifts of the M reflecting elements are designed to constructively combine the direct and RIS-reflective (i.e., indirect) signals. Then, an RIS enhances the signal-to-interference-plus-noise ratio (SINR) at D. Both a direct channel (from S to D) and a RIS-reflective channel (i.e., from S to D via an RIS) are considered to facilitate the high SINR requirements at D.

---

[1]In a simpler RIS setup with subwavelength-sized reflecting elements, a phase shift can be obtained by adjusting the bias voltage applied to the tunable capacitor and a variable resistor is added to change the amplitude. In such a way, we can control the reflection coefficient (i.e., amplitude and phase shift) of each reflecting element individually.

B. CHANNEL MODELING

The path loss is used to analyse the large scale attenuations in an RIS-embedded environment [31]. Taking into account the area of an RIS, the placement of the RIS plane and phase-aligning the reflected signals of the reflecting elements towards a target angle θ_R (i.e., in the direction of D), the pathloss via an RIS at the far-field distance can be expressed by

$$L_{RIS} = \frac{G_1 G_2}{(4\pi)^2} \frac{(X_R Y_R)^2}{(d_1 d_2)^2} \cos^2(\theta_i - \theta_{Rot}), \quad (1)$$

where θ_i and θ_{Rot} are the incident angle of the signal and the rotation angle of an RIS plane, respectively. G_1 and G_2 are the antenna gains at S and D, respectively. X_R and Y_R are the aggregate length and width of the RIS having M reflecting elements, respectively. Since the reflecting elements are deployed in an end-to-end configuration, the area (size) of the RIS is given by $X_R Y_R = Ml^2$ where l is the side length (horizontal width and vertical height) of the square reflecting element. Furthermore, the effective area of the RIS as seen from the S is given by $X_R Y_R \cos(\theta_i - \theta_{Rot})$, i.e., $\theta_{Rot} = 0$ if the RIS plane is vertically straight.

We consider the tractable independent and identically distributed (i.i.d.) Rayleigh model for small-scale multipath fading to provide an upper bound performance [32], [33]. In detail, the channel coefficients from S to D, from S to mth reflecting element and from mth reflecting element to D
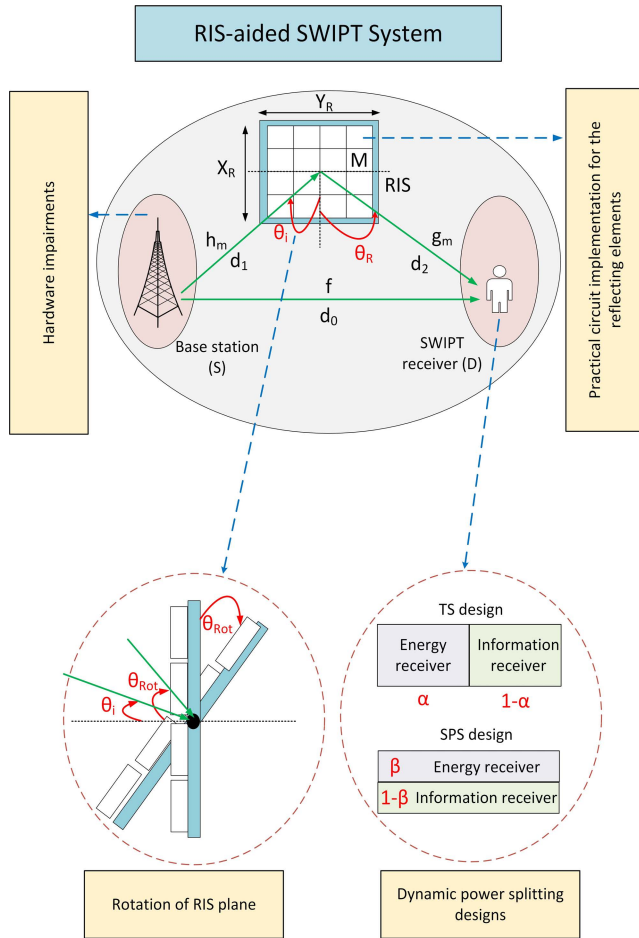
FIGURE 1. An illustration of RIS-aided SWIPT systems.

are represented in polar form as $f = f_a e^{j\theta_f}$, $h_m = \alpha_m e^{j\theta_m}$ and $g_m = \kappa_m e^{j\epsilon_m}$, respectively. The phases (i.e., θ_f, θ_m and ϵ_m) are uniformly distributed in the interval $[-\pi, \pi)$. For simplicity, the channel gains (i.e., $|f|^2$, $|h_m|^2$ and $|g_m|^2$ follow an Exponential distribution with parameter 1. We follow a generic assumption of the channel state information (CSI), i.e., RIS has the phase information of all the channels.[2] Furthermore, the channels are assumed to be static for a transmission in each block [35], [36].[3] Note that the path-loss is not included in the small-scale fading coefficients since it is implicitly taken into account in Eq. (1).

C. PHASE SHIFT MODEL
The reflection coefficient for the mth reflecting element of the RIS is defined by $\chi_m \triangleq \psi_m e^{j\phi_m}$, where $\phi_m \in [-\pi, \pi)$

---

[2]The RIS-cascaded channel can be estimated via active transceivers at S and D, i.e., by transmitting and receiving the pilots, for a fixed configuration of the reflecting elements [34]. The nearby elements can be in the same group to reduce the computational complexity at the expense of channel estimation error and the performance degradation. However, the detailed channel estimation procedure is outside the scope of this paper.

[3]The quasi-static channels are practically feasible for SWIPT systems owing to the stationary and/or low mobility environments, e.g., the indoor scenarios with fixed short-range coverage area.

and $\psi_m \in [0, 1]$ are the phase shift and reflection amplitude, respectively. In ideal phase shifting [37], the optimal reflection design considers a constant reflection amplitude regardless of the phase shift, i.e., $\psi_m = 1$. In practice, the amplitude and phase responses of the RIS depend on the circuit implementation of the reflecting elements. The amplitude response is non-uniform with respect to its phase shift, i.e., the amplitude response is a function of phase. In detail, the reflection amplitude for the practical phase shifters exhibits the minimum value with the phase shift setting near zero and the maximum value with the phase shift setting around π or $-\pi$. Therefore, the phase shifting around π or $-\pi$ can only maximize the effective channel power gain [38]. In this respect, we present the analytical phase shift model to characterize the intertwined relationship for the amplitude and phase response of each reflecting element and capture the phase-dependent amplitude variation in the element-wise reflection coefficient, i.e., $\chi_m \triangleq \psi_m(\phi_m) e^{j\phi_m}$. Specifically, $\psi_m(\phi_m)$ is defined as

$$\psi_m(\phi_m) = (1 - \psi_{min}) \left(\frac{\sin(\phi_m - \varpi) + 1}{2} \right)^\vartheta + \psi_{min}, \quad (2)$$

where $\psi_{min} \geq 0$, $\vartheta \geq 0$ and $\varpi \geq 0$ are the constants related to the hardware implementation of the reflecting elements and are determined by a standard curve fitting tool. Then, a setting $\psi_{min} = 1$ (or $\vartheta = 0$) employs the ideal phase shifting.

D. SIGNAL TRANSMISSION MODEL
The RTHIs can be modeled as the additive distortion noise to make the analysis mathematically traceable. With transmit power for S bounded by P_S, the baseband equivalent received signal at D can be written as

$$y[n] = \left(\sqrt{L_0} f + \sqrt{L_{RIS}} \sum_{m=1}^{M} h_m \chi_m g_m \right) \times \left(\sqrt{P_S} x_T[n] + \omega_S[n] \right) + \omega_D[n] + n_D[n], \quad (3)$$

where $x_T[n]$ is the Gaussian modulated signal with unit energy (i.e., $\mathbb{E}\{|x_T|^2\} = 1$) at symbol time n and $n_D[n] \sim \mathcal{CN}(0, \sigma^2)$ is an additive white Gaussian noise (AWGN) [39]. Furthermore, $L_0 = \frac{G_1 G_2 \lambda^2}{(4\pi d_0)^2}$ represents the pathloss for a direct link from S to D; d_0 is the distance from S to D. $\omega_S[n] \sim \mathcal{CN}(0, \zeta_S^2 P_S)$ and $\omega_D[n] \sim \mathcal{CN}\left(0, \zeta_D^2 |L_0 f + L_{RIS} \sum_{m=1}^{M} h_m \chi_m g_m|^2 P_S\right)$ are the distortion noises at S and D, respectively. Combining the distribution of $\omega_S[n]$ and $\omega_D[n]$ after some mathematical calculations, the received signal at D can be rewritten as

$$y[n] = \left(\sqrt{L_0} f + \sqrt{L_{RIS}} \sum_{m=1}^{M} h_m \chi_m g_m \right) \times \left(\sqrt{P_S} x_T[n] + \omega_T[n] \right) + n_D[n], \quad (4)$$

where $\omega_T[n] \sim \mathcal{CN}(0, \zeta_T^2 P_S)$ is an aggregate distortion noise and is the sum of effective distortion noises

$\omega_S[n]$ and $\omega_D[n] \left| L_0 f + L_{RIS} \sum_{m=1}^{M} h_m \chi_m g_m \right|^{-2}$. Here, $\zeta_T = \sqrt{\zeta_S^2 + \zeta_D^2}$ represents the RTHI level.

Furthermore, the effective channel power gain considering the two links, i.e., S to D and S to D via RIS, is given by $\left| \sqrt{L_0} f_a e^{j\theta_f} + \sqrt{L_{RIS}} \sum_{m=1}^{M} \alpha_m \kappa_m e^{(\phi_m + \theta_m + \epsilon_m)} \psi_m(\phi_m) \right|^2$. We align the common phase of the RIS with that of the direct path by setting $\phi_m^* = \theta_f - (\theta_m + \epsilon_m)$ [40]. Consequently, the effective channel power can be rewritten as $\left| \sqrt{L_0} f_a e^{j\theta_f} + \sqrt{L_{RIS}} \sum_{m=1}^{M} \alpha_m \kappa_m \psi_m(\phi_m^*) \right|^2$.

III. PERFORMANCE ANALYSIS
A. POWER AND TIME SPLITTING DESIGNS
To implement the SWIPT receiver D, we consider the power and time splitting designs with the adjustable power and time ratios and a separated receiver architecture (i.e., a separate information and energy receiver). In a SPS operation mode, D harvests energy and decodes information by splitting the received signal $y[n]$ into two streams with the arbitrary power splitting factor β for the whole packet interval, where $0 \leq \beta \leq 1$. In detail, assuming that each packet consists of K symbols, $\sqrt{\beta} y[n]$ and $\sqrt{1 - \beta} y[n]$ are used for EH and ID for $i = 1, \cdots, K$. On the other hand, in a TS operation mode, D harvests energy with the first αK symbols, i.e., $y[n]$ for $n = 1, \cdots, \alpha K$, and D decodes information with the remaining $(1-\alpha)K$ symbols, i.e., $y[n]$ for $n = \alpha K + 1, \cdots, K$. Note that we only consider α such that αK becomes a positive integer.

B. ACHIEVABLE RATES-RESIDUAL ENERGY TRADEOFFS
The residual energy is the net stored energy in a battery, i.e., the harvested energy minus the consumed energy. For the sake of the clarity in the performance analysis with the useful insights, we consider a simplified linear EH model, i.e., the harvested energy increases linearly with the received power and therefore, the energy conversion efficiency (η) is constant [41]. The corresponding residual energy for the TS and SPS operating modes can be represented as

$$
\begin{aligned}
&E_R^{TS}(\alpha) \\
&= \alpha \eta P_S \left(1 + \zeta_T^2 \right) \\
&\quad \times \left| \sqrt{L_0} f_a + \sqrt{L_{RIS}} \sum_{m=1}^{M} \alpha_m \kappa_m \psi_m(\phi_m^*) \right|^2 - (1-\alpha)P_C,
\end{aligned}
\tag{5}
$$

and

$$
\begin{aligned}
&E_R^{SPS}(\beta) \\
&= \beta \eta P_S \left(1 + \zeta_T^2 \right) \\
&\quad \times \left| \sqrt{L_0} f_a + \sqrt{L_{RIS}} \sum_{m=1}^{M} \alpha_m \kappa_m \psi_m(\phi_m^*) \right|^2 - P_C, \tag{6}
\end{aligned}
$$

respectively, where P_C is the fixed circuit power dissipated by the information receiver.[3] Here, we assume the negligible power consumption for the energy receiver due to the passive devices, such as Schottky diode and low-pass filters, etc.

For TS and SPS modes, the SINRs to extract x_T at D for the TS and SPS modes can be expressed as

$$
\begin{aligned}
&SINR^{TS} \\
&= \frac{\left| \sqrt{L_0} f_a + \sqrt{L_{RIS}} \sum_{m=1}^{M} \alpha_m \kappa_m \psi_m(\phi_m^*) \right|^2 \rho_S}{\left| \sqrt{L_0} f_a + \sqrt{L_{RIS}} \sum_{m=1}^{M} \alpha_m \kappa_m \psi_m(\phi_m^*) \right|^2 \rho_S \zeta_T^2 + 1},
\end{aligned}
\tag{7}
$$

and

$$
\begin{aligned}
&SINR^{SPS} \\
&= \frac{(1-\beta) \left| \sqrt{L_0} f_a + \sqrt{L_{RIS}} \sum_{m=1}^{M} \alpha_m \kappa_m \psi_m(\phi_m^*) \right|^2 \rho_S}{(1-\beta) \left| \sqrt{L_0} f_a + \sqrt{L_{RIS}} \sum_{m=1}^{M} \alpha_m \kappa_m \psi_m(\phi_m^*) \right|^2 \rho_S \zeta_T^2 + 1},
\end{aligned}
\tag{8}
$$

respectively, where $\rho_S = \frac{P_S}{\sigma^2}$.

The corresponding achievable rates for the TS and SPS modes can be obtained by

$$
\begin{aligned}
&R_A^{TS}(\alpha) \\
&= (1 - \alpha) \log_2(1 + SINR^{TS}) \\
&= (1-\alpha) \log_2 \\
&\times \left(1 + \frac{\left| \sqrt{L_0} f_a + \sqrt{L_{RIS}} \sum_{m=1}^{M} \alpha_m \kappa_m \psi_m(\phi_m^*) \right|^2 \rho_S}{\left| \sqrt{L_0} f_a + \sqrt{L_{RIS}} \sum_{m=1}^{M} \alpha_m \kappa_m \psi_m(\phi_m^*) \right|^2 \rho_S \zeta_T^2 + 1} \right),
\end{aligned}
\tag{9}
$$

and

$$
\begin{aligned}
&R_A^{SPS}(\beta) \\
&= \log_2(1 + SINR^{SPS}) \\
&= \log_2 \\
&\times \left(1 + \frac{(1-\beta) \left| \sqrt{L_0} f_a + \sqrt{L_{RIS}} \sum_{m=1}^{M} \alpha_m \kappa_m \psi_m(\phi_m^*) \right|^2 \rho_S}{(1-\beta) \left| \sqrt{L_0} f_a + \sqrt{L_{RIS}} \sum_{m=1}^{M} \alpha_m \kappa_m \psi_m(\phi_m^*) \right|^2 \rho_S \zeta_T^2 + 1} \right),
\end{aligned}
\tag{10}
$$

respectively.

For simple expression and further investigation, let $W = \left| \sqrt{L_0} f_a + \sqrt{L_{RIS}} \sum_{m=1}^{M} \alpha_m \kappa_m \psi_m(\phi_m^*) \right|^2$, $k_1 = \eta P_S \left(1 + \zeta_T^2 \right)$, $k_2 = \rho_S$, and $k_3 = k_2 \zeta_T^2$. It can be expected that there exists a tradeoff between the achievable rate and residual energy, i.e., R-Er tradeoff, for the TS and SPS modes depending on the splitting factors α and β. For explicit

---

expression for such tradeoff, achievable rates for both operating modes are written as functions of the residual energy as follows:

$$R_A{}^{TS}(E_R{}^{TS}) = \left(1 - \frac{P_C + E_R{}^{TS}}{P_C + k_1 W}\right) \log_2\left(1 + \frac{Wk_2}{Wk_3 + 1}\right), \quad (11)$$

and

$$R_A{}^{SPS}(E_R{}^{SPS})$$
$$= \log_2\left(1 + \frac{\frac{k_2}{k_1}\left(k_1 W - P_C - E_R{}^{SPS}\right)}{\frac{k_3}{k_1}\left(k_1 W - P_C - E_R{}^{SPS}\right) + 1}\right), \quad (12)$$

respectively.

First, we provide the statistical characterization of $W = \left|\sqrt{L_0}f_a + \sqrt{L_{RIS}}\sum_{m=1}^{M}\alpha_m\kappa_m\psi_m(\phi_m^*)\right|^2$. Given both α_m and κ_m following the Rayleigh distributions, the CDF of $\alpha_m\kappa_m$ can be represented as

$$F_{\alpha_m\kappa_m}(z) = Pr(\alpha_m\kappa_m < z) = Pr\left(\alpha_m < \frac{z}{\kappa_m} = \frac{z}{v}\right)$$
$$= \int_0^\infty F_{\alpha_m}\left(\frac{z}{v}\right)f_{\kappa_m=v}(v)\,dv = 1 - 2zK_1(2z), \quad (13)$$

where $K_n(.)$ is the modified Bessel function of second kind with n^{th} order [42, Eq. (8.407)].

Using Eq. (13), the PDF of $\alpha_m\kappa_m$ is then computed as

$$f_{\alpha_m\kappa_m}(z) = \frac{dF_{\alpha_m\kappa_m}(z)}{dz}$$
$$= 2z\{K_2(2z) - K_0(2z)\} - 2K_1(2z). \quad (14)$$

By utilizing Eq. (14) and [42, Eq. (8.486.11)], we can compute the statistical information of $\alpha_m\kappa_m$ in terms of the expectation and the variance as $\mathbb{E}\{\alpha_m\kappa_m\} = \frac{\pi}{4}$ and $\mathbb{V}\{\alpha_m\kappa_m\} = 1 - \frac{\pi^2}{16}$, respectively.

Further, ϕ_m^* is uniformly distributed in $[-\pi, \pi]$. For $X = \phi_m^* \sim \mathcal{U}(-\pi, \pi)$, the PDF of X is $f_X(x) = \frac{1}{2\pi}$. For $Y = \sin(x)$, the real roots of $g(x) = y$ are $x_1 = \sin^{-1}(y)$ and $x_2 = \pi - \sin^{-1}(y)$. Then, the PDF of $Y = g(x)$ can be determined as

$$f_Y(y) = \frac{f_X(x_1)}{g'(x_1)} + \frac{f_X(x_2)}{g'(x_2)}$$
$$= \frac{1}{2\pi\cos(\sin^{-1}(y))} + \frac{1}{2\pi\cos(\pi - \sin^{-1}(y))}$$
$$= \begin{cases} \frac{1}{\pi\sqrt{1-y^2}}, & \text{if } |y| < 1, \\ 0, & \text{otherwise.} \end{cases} \quad (15)$$

Using Eq. (15) and the transformation method, the PDF of $\psi_m(\phi_m^*)$ for $\psi_{min} \neq 1$, and $\vartheta \neq 0$ can be formulated as

$$f_{\psi_m(\phi_m^*)}(q) = \frac{\left(\frac{q-\psi_{min}}{1-\psi_{min}}\right)^{\frac{1}{\vartheta}-1}}{\pi\vartheta(1-\psi_{min})\sqrt{\left(\frac{q-\psi_{min}}{1-\psi_{min}}\right)^{\frac{1}{\vartheta}} - \left(\frac{q-\psi_{min}}{1-\psi_{min}}\right)^{\frac{2}{\vartheta}}}}, \quad (16)$$

where $q \in (\psi_{min}, 1)$.

Using Eq. (16), we derive the first moment of $\psi_m(\phi_m^*)$, $X_A \triangleq \mathbb{E}\{\psi_m(\phi_m^*)\}$ as

$$X_A = \int_0^\infty q f_{\psi_m(\phi_m^*)}(q)$$
$$= \frac{1}{\pi\vartheta(1-\psi_{min})}\int_{\psi_{min}}^1 \frac{q\left(\frac{q-\psi_{min}}{1-\psi_{min}}\right)^{\frac{1}{\vartheta}-1}}{\sqrt{\left(\frac{q-\psi_{min}}{1-\psi_{min}}\right)^{\frac{1}{\vartheta}} - \left(\frac{q-\psi_{min}}{1-\psi_{min}}\right)^{\frac{2}{\vartheta}}}}\,dq$$
$$= \frac{(1-\psi_{min})\Gamma\left(\vartheta+\frac{1}{2}\right)\Gamma\left(\frac{1}{2}\right)}{\pi\Gamma(\vartheta+1)}, \quad (17)$$

where $\Gamma(.)$ is the Gamma function defined by the Euler integral [42, Eq. (8.310)].

Following a similar procedure, we derive the second moment of $\psi_m(\phi_m^*)$, $X_C \triangleq \mathbb{E}\{|\psi_m(\phi_m^*)|^2\}$ as

$$X_C = \left(\frac{(1-\psi_{min})^2}{\pi}\right)\frac{\Gamma\left(2\vartheta+\frac{1}{2}\right)\Gamma\left(\frac{1}{2}\right)}{\Gamma(2\vartheta+1)}$$
$$+ \psi_{min}^2 + \left(\frac{2\psi_{min}(1-\psi_{min})}{\pi}\right)\frac{\Gamma\left(\vartheta+\frac{1}{2}\right)\Gamma\left(\frac{1}{2}\right)}{\Gamma(\vartheta+1)}. \quad (18)$$

Using Eqs. (17) and (18), we derive the variance of $\psi_m(\phi_m^*)$, $X_B \triangleq X_C - (X_A)^2$ as follows:

$$X_B = \frac{(1-\psi_{min})^2\Gamma\left(2\vartheta+\frac{1}{2}\right)\Gamma\left(\frac{1}{2}\right)}{\pi\Gamma(2\vartheta+1)}$$
$$- \frac{(1-\psi_{min})^2\Gamma^2\left(\vartheta+\frac{1}{2}\right)\Gamma^2\left(\frac{1}{2}\right)}{\pi^2\Gamma^2(\vartheta+1)}. \quad (19)$$

For a sufficiently large number of reflecting elements, i.e., $M \gg 1$, $\sum_{m=1}^{M}\alpha_m\kappa_m\psi_m(\phi_m^*)$ converges to a Gaussian distributed $\mathcal{RV}$, and its statistical information can be determined by the independent $\mathcal{RV}s$ $\alpha_m\kappa_m$ and $\psi_m(\phi_m^*)$. The expectation and the variance of $\sum_{m=1}^{M}\alpha_m\kappa_m\psi_m(\phi_m^*)$ can be determined as

$$\mathbb{E}\left\{\sum_{m=1}^{M}\alpha_m\kappa_m\psi_m(\phi_m^*)\right\} = \sum_{m=1}^{M}\mathbb{E}\{\alpha_m\kappa_m\}\mathbb{E}\{\psi_m(\phi_m^*)\}$$
$$= M\frac{\pi}{4}X_A, \quad (20)$$

and

$$\mathbb{V}\left\{\sum_{m=1}^{M}\alpha_m\kappa_m\psi_m(\phi_m^*)\right\}$$
$$= \sum_{m=1}^{M}\mathbb{V}\{\alpha_m\kappa_m\}\mathbb{V}\{\psi_m(\phi_m^*)\} + \mathbb{V}\{\alpha_m\kappa_m\}\left(\mathbb{E}\{\psi_m(\phi_m^*)\}\right)^2$$
$$+ \mathbb{V}\{\psi_m(\phi_m^*)\}\left(\mathbb{E}\{\alpha_m\kappa_m\}\right)^2$$
$$= M\left\{\left(1 - \frac{\pi^2}{16}\right)X_B + \left(1 - \frac{\pi^2}{16}\right)(X_A)^2 + \left(\frac{\pi}{4}\right)^2 X_B\right\}, \quad (21)$$

respectively.

Based on the above results, it can be seen that $W = |\sqrt{L_0}f_a + \sqrt{L_{RIS}} \sum_{m=1}^{M} \alpha_m \kappa_m \psi_m (\phi_m^*)|^2$ is a square of a sum of a Gaussian and a Rayleigh distributed $\mathcal{RV}$s. To provide the fitting of the complicated distribution, we consider the regular Gamma distribution, i.e, $W \overset{.}{\sim} \Gamma(k_W, w_W)$, where k_W and w_W are the shape parameter and the scale parameter of W, respectively. It follows immediately that the shape and the scale parameters can be determined using the moment matching technique. The exact first and second moments of W can be determined by

$$\mathbb{E}\{W\} = L_0 \mathbb{E}\{|f_a|^2\} + L_{RIS} \mathbb{E}\left\{\left|\sum_{m=1}^{M} \alpha_m \kappa_m \psi_m (\phi_m^*)\right|^2\right\}$$
$$+ 2\sqrt{L_0}\sqrt{L_{RIS}} \mathbb{E}\{f_a\} \mathbb{E}\left\{\sum_{m=1}^{M} \alpha_m \kappa_m \psi_m (\phi_m^*)\right\}, \quad (22)$$

and

$$\mathbb{E}\{W^2\} = \sum_{t=0}^{4} \binom{4}{t} \left(\sqrt{L_0}\right)^t \left(\sqrt{L_{RIS}}\right)^{4-t}$$
$$\times \mathbb{E}\{|f_a|^t\} \mathbb{E}\left\{\left|\sum_{m=1}^{M} \alpha_m \kappa_m \psi_m (\phi_m^*)\right|^{4-t}\right\}, \quad (23)$$

respectively, where

$$\mathbb{E}\{|f_a|^4\} = 2, \quad (24)$$

$$\mathbb{E}\{|f_a|^3\} = \frac{3\sqrt{\pi}}{4}, \quad (25)$$

$$\mathbb{E}\{|f_a|^2\} = \mathbb{V}\{f_a\} + (\mathbb{E}\{f_a\})^2$$
$$= \frac{4-\pi}{4} + \left(\frac{\sqrt{\pi}}{2}\right)^2 = 1, \quad (26)$$

$$\mathbb{E}\{f_a\} = \frac{\sqrt{\pi}}{2}, \quad (27)$$

$$\mathbb{E}\left\{\left|\sum_{m=1}^{M} \alpha_m \kappa_m \psi_m (\phi_m^*)\right|^2\right\} = \left(\mathbb{E}\left\{\sum_{m=1}^{M} \alpha_m \kappa_m \psi_m (\phi_m^*)\right\}\right)^2$$
$$+ \mathbb{V}\left\{\sum_{m=1}^{M} \alpha_m \kappa_m \psi_m (\phi_m^*)\right\}$$
$$= M\left\{X_B + \left(1 - \frac{\pi^2}{16}\right)(X_A)^2\right\}$$
$$+ \left(M\frac{\pi}{4}X_A\right)^2, \quad (28)$$

$$\mathbb{E}\left\{\left|\sum_{m=1}^{M} \alpha_m \kappa_m \psi_m (\phi_m^*)\right|^3\right\} = \left(\mathbb{E}\left\{\sum_{m=1}^{M} \alpha_m \kappa_m \psi_m (\phi_m^*)\right\}\right)^3$$
$$+ 3\mathbb{E}\left\{\sum_{m=1}^{M} \alpha_m \kappa_m \psi_m (\phi_m^*)\right\}$$
$$\times \mathbb{V}\left\{\sum_{m=1}^{M} \alpha_m \kappa_m \psi_m (\phi_m^*)\right\}$$

$$= M^2\left\{M\left(\frac{\pi}{4}X_A\right)^3 + \frac{3\pi}{4}X_A\{X_B$$
$$+ \left(1 - \frac{\pi^2}{16}\right)(X_A)^2\}\right\}, \quad (29)$$

and

$$\mathbb{E}\left\{\left|\sum_{m=1}^{M} \alpha_m \kappa_m \psi_m (\phi_m^*)\right|^4\right\}$$
$$= \left(\mathbb{E}\left\{\sum_{m=1}^{M} \alpha_m \kappa_m \psi_m (\phi_m^*)\right\}\right)^4$$
$$+ 6\left(\mathbb{E}\left\{\sum_{m=1}^{M} \alpha_m \kappa_m \psi_m (\phi_m^*)\right\}\right)^2 \mathbb{V}\left\{\sum_{m=1}^{M} \alpha_n \kappa_m \psi_m (\phi_m^*)\right\}$$
$$+ 3\left(\mathbb{V}\left\{\sum_{m=1}^{M} \alpha_m \kappa_m \psi_m (\phi_m^*)\right\}\right)^2$$
$$= \left(M\frac{\pi}{4}X_A\right)^4 + 6M\left(M\frac{\pi}{4}X_A\right)^2\left\{X_B + \left(1 - \frac{\pi^2}{16}\right)(X_A)^2\right\}$$
$$+ 3M^2\left\{X_B + \left(1 - \frac{\pi^2}{16}\right)(X_A)^2\right\}^2. \quad (30)$$

Using the statistics associated with a Rayleigh distributed f_a and a Gaussian distributed $\sum_{m=1}^{M} \alpha_m \kappa_m \psi_m (\phi_m^*)$, which are given in Eqs. (24)-(30), we solve Eqs. (22) and (23) as follows:

$$\mathbb{E}\{W\} = \sqrt{L_0}\sqrt{L_{RIS}}$$
$$\times \left(MX_B + M\frac{\pi\sqrt{\pi}}{4}X_A + M\left(1 - \frac{\pi^2}{16}\right)(X_A)^2\right)$$
$$+ L_{RIS}\left(M\frac{\pi}{4}X_A\right)^2 + L_0, \quad (31)$$

and

$$\mathbb{E}\{W^2\}$$
$$= (L_{RIS})^2$$
$$\times \left(\left(M\frac{\pi}{4}X_A\right)^4 + 6M\left(M\frac{\pi}{4}X_A\right)^2\left\{X_B + \left(1 - \frac{\pi^2}{16}\right)(X_A)^2\right\}\right)$$
$$+ 3(ML_{RIS})^2\left\{X_B + \left(1 - \frac{\pi^2}{16}\right)(X_A)^2\right\}^2$$
$$+ 2M^2\sqrt{\pi L_0}\left(\sqrt{L_{RIS}}\right)^3$$
$$\times \left\{M\left(\frac{\pi}{4}X_A\right)^3 + \frac{3\pi}{4}X_A\left\{X_B + \left(1 - \frac{\pi^2}{16}\right)(X_A)^2\right\}\right\}$$
$$+ L_0 L_{RIS}\left(6M\left\{X_B + \left(1 - \frac{\pi^2}{16}\right)(X_A)^2\right\} + 6\left(M\frac{\pi}{4}X_A\right)^2\right)$$
$$+ 3\left(\sqrt{L_0}\right)^3 \sqrt{L_{RIS}}\sqrt{\pi}M\frac{\pi}{4}X_A + 2(L_0)^2, \quad (32)$$

respectively.

Using the first and second moment statistics obtained in Eqs. (31) and (32), we can determine k_W and w_W as

$$k_W = \frac{(\mathbb{E}\{W\})^2}{\mathbb{E}\{W^2\} - (\mathbb{E}\{W\})^2}, \tag{33}$$

and

$$w_W = \frac{\mathbb{E}\{W^2\} - (\mathbb{E}\{W\})^2}{\mathbb{E}\{W\}}, \tag{34}$$

respectively. To present the analytical framework deriving the tight bounds for the achievable information rate, residual energy, and R-Er tradeoff for TS and SPS designs, we use the following necessary Lemmas.

Lemma 1: For positive u_1, u_2 and u_3

$$\log_2\left(1 + \frac{u_1}{u_2 + u_3}\right) = \log_2\left(1 + \frac{u_1 + u_2}{u_3}\right) - \log_2\left(1 + \frac{u_2}{u_3}\right) \tag{35}$$

Proof: The proof is available in [43]. □

Lemma 2: If X is a $\mathcal{RV}$ with the expectation $\mathbb{E}\{X\}$ and the variance $\mathbb{V}\{X\}$, the improved approximation for $\mathbb{E}\{\ln(1 + X)\}$ using the Taylor expansion can be derived as,

$$\mathbb{E}\{\ln(1 + X)\} \approx \ln(1 + \mathbb{E}\{X\}) - \frac{\mathbb{V}\{X\}}{2(1 + \mathbb{E}\{X\})^2} \tag{36}$$

Proof: The proof is available in [43]. □

Lemma 3: Further, the improved approximation for $\mathbb{E}\{X = \frac{A}{B}\}$ using the Taylor expansion can be derived as,

$$\mathbb{E}\left\{\frac{A}{B}\right\} \approx \frac{\mathbb{E}\{A\}}{\mathbb{E}\{B\}} + \frac{\mathbb{E}\{A\}\mathbb{V}\{B\}}{(\mathbb{E}\{B\})^3} \tag{37}$$

Proof: The proof is available in [44], [45]. □

Lemma 4: For $a_1 > 0$, $b_1 > 0$ and $Y \stackrel{\sim}{} \Gamma(k_Y, w_Y)$, the expectation and the variance of $a_1 + b_1 Y$ are respectively given by

$$\mathbb{E}\{a_1 + b_1 Y\} = a_1 + k_Y b_1 w_Y, \tag{38}$$

$$\mathbb{V}\{a_1 + b_1 Y\} = k_Y (b_1 w_Y)^2 \tag{39}$$

Proof: The proof is available in [46], [47]. □

Using Lemma 1, the average residual energy, average achievable information rate, and R-Er tradeoff for the TS design can be respectively calculated as

$$\overline{E_R^{TS}}(\alpha) = \mathbb{E}\left\{E_R^{TS}(\alpha)\right\}$$
$$= \mathbb{E}\{\alpha k_1 W - (1 - \alpha)P_C\}, \tag{40}$$

$$\overline{R_A^{TS}}(\alpha) = \mathbb{E}\left\{R_A^{TS}(\alpha)\right\}$$
$$= (1 - \alpha)(\mathbb{E}\{\log_2(1 + W(k_2 + k_3))$$
$$- \log_2(1 + Wk_3)\}, \tag{41}$$

$$\overline{R_A^{TS}}(\overline{E_R^{TS}}) = \mathbb{E}\left\{R_A^{TS}(E_R^{TS})\right\}$$
$$= \mathbb{E}\left\{\left(\frac{k_1 W - \overline{E_R^{TS}}}{k_1 W + P_C}\right)\right\}$$
$$\times \mathbb{E}\left\{(\log_2(1 + W(k_2 + k_3))$$
$$- \log_2(1 + Wk_3))\right\}, \tag{42}$$

Using Lemmas 2-4, the tight bounds for the average achievable information rate and R-Er tradeoff for the TS design can be respectively derived as,

$$\overline{E_R^{TS}}(\alpha) = k_W \alpha k_1 w_W - (1 - \alpha)P_C, \tag{43}$$

$$\overline{R_A^{TS}}(\alpha) \approx \frac{(1 - \alpha)}{\ln 2}(T_1 - T_2), \tag{44}$$

$$\overline{R_A^{TS}}(\overline{E_R^{TS}}) \approx \frac{T_0}{\ln 2}(T_1 - T_2), \tag{45}$$

where

$$T_0 = \left(k_W k_1 w_W - \overline{E_R^{TS}}\right)$$
$$\times \left(\frac{1}{k_W k_1 w_W + P_C} + \frac{k_W (k_1 w_W)^2}{(k_W k_1 w_W + P_C)^3}\right), \tag{46}$$

$$T_1 = \ln\left(\frac{1 + k_W (k_2 + k_3) w_W}{1 + k_W k_3 w_W}\right), \tag{47}$$

$$T_2 = \frac{k_W ((k_2 + k_3) w_W)^2}{2(1 + k_W (k_2 + k_3) w_W)^2} - \frac{k_W (k_3 w_W)^2}{2(1 + k_W k_3 w_W)^2}, \tag{48}$$

Now, the average residual energy, average achievable information rate, and R-Er tradeoff for the SPS design can be respectively calculated as

$$\overline{E_R^{SPS}}(\beta)$$
$$= \mathbb{E}\left\{E_R^{SPS}(\beta)\right\}$$
$$= \mathbb{E}\{\beta k_1 W - P_C\}, \tag{49}$$

$$\overline{R_A^{SPS}}(\beta)$$
$$= \mathbb{E}\left\{R_A^{SPS}(\beta)\right\}$$
$$= \mathbb{E}\{\log_2(1 + W(1 - \beta)(k_2 + k_3)) - \log_2(1 + W(1 - \beta)k_3)\}, \tag{50}$$

$$\overline{R_A^{SPS}}(\overline{E_R^{SPS}})$$
$$= \mathbb{E}\left\{R_A^{SPS}(E_R^{SPS})\right\}$$
$$= \mathbb{E}\left\{\log_2\left(1 + \left(\frac{k_2 + k_3}{k_1}\right)\left(k_1 W - \overline{E_R^{SPS}} - P_C\right)\right)\right\}$$
$$- \mathbb{E}\left\{\log_2\left(1 + \left(\frac{k_3}{k_1}\right)\left(k_1 W - \overline{E_R^{SPS}} - P_C\right)\right)\right\}, \tag{51}$$

Using Lemmas 2-4, the tight bounds for the average achievable information rate and R-Er tradeoff for the SPS design can be finally expressed as,

$$\overline{E_R^{SPS}}(\beta) = k_W \beta k_1 w_W - P_C, \tag{52}$$

$$\overline{R_A^{SPS}}(\beta) \approx \frac{1}{\ln 2}(T_4 - T_5), \tag{53}$$

$$\overline{R_A^{SPS}}(\overline{E_R^{SPS}}) \approx \frac{1}{\ln 2}(T_6 - T_7), \tag{54}$$

where

$$T_4 = \ln\left(\frac{1 + k_W (1 - \beta)(k_2 + k_3) w_W}{1 + k_W (1 - \beta)k_3 w_W}\right), \tag{55}$$

$$T_5 = \frac{k_w \left((1-\beta)(k_2+k_3)\, w_w\right)^2}{2\left(1+k_w\,(1-\beta)(k_2+k_3)\, w_w\right)^2}$$
$$- \frac{k_w \left((1-\beta)k_3 w_w\right)^2}{2\left(1+k_w\,(1-\beta)\, k_3 w_w\right)^2}, \tag{56}$$

$$T_6 = \ln\left(\frac{1+\left(k_w\,(k_2+k_3)\, w_w - \frac{(k_2+k_3)}{k_1}\left(\overline{E_R^{SPS}}+P_C\right)\right)}{1+\left(k_w k_3 w_w - \frac{k_3}{k_1}\left(\overline{E_R^{SPS}}+P_C\right)\right)}\right), \tag{57}$$

$$T_7 = \frac{k_w \left((k_2+k_3)\, w_w\right)^2}{2\left(1+\left(k_w\,(k_2+k_3)\, w_w - \frac{(k_2+k_3)}{k_1}\left(\overline{E_R^{SPS}}+P_C\right)\right)\right)^2}$$
$$- \frac{k_w \left(k_3 w_w\right)^2}{2\left(1+\left(k_w k_3 w_w - \frac{k_3}{k_1}\left(\overline{E_R^{SPS}}+P_C\right)\right)\right)^2}, \tag{58}$$

IV. EXTENSION TO RIS CORRELATED CHANNELS AND NON-LINEAR EH MODEL

In the previous sections, we investigate the R-Er tradeoffs for TS and SPS designs under i.i.d. Rayleigh fading and a linear EH model. In this section, we discuss the approach to extend to the general cases, i.e., spatial correlation in RIS channels and non-linear behavior of EH circuit.

In an isotropic scattering environment, the spatial correlation cannot be avoided for the RIS having practical reflecting elements with sub-wavelength-sized [48]. Taking into account the general correlated Rayleigh fading model for the RIS-aided communications, the indirect RIS channels are presented as $h = [h_1, \cdots, h_m]^T \sim \mathcal{CN}(0, R_S)$ and $g = [g_1, \cdots, g_m]^T \sim \mathcal{CN}(0, R_D)$, where R_S and R_D represent the spatial correlation matrix of the channels from S to RIS and RIS to D, respectively. The received signal at D can be rewritten by

$$y_c[n] = \left(\sqrt{L_0}f + \sqrt{L_{RIS}}h^H X g\right)$$
$$\times \left(\sqrt{P_S}x_T[n] + \omega_S[n]\right) + \omega_D[n] + n_D[n], \tag{59}$$

where $X = \text{diag}\,(\chi_1, \cdots, \chi_m)$ is the diagonal phase-shift matrix determining the configuration of the RIS. Then, the SINR for TS and SPS modes can be expressed by

$$SINR_c^{TS} = \frac{\left|\sqrt{L_0}f + \sqrt{L_{RIS}}h^H X g\right|^2 \rho_S}{\left|\sqrt{L_0}f + \sqrt{L_{RIS}}h^H X g\right|^2 \rho_S \zeta_T^2 + 1}, \tag{60}$$

and

$$SINR_c^{SPS} = \frac{(1-\beta)\left|\sqrt{L_0}f + \sqrt{L_{RIS}}h^H X g\right|^2 \rho_S}{(1-\beta)\left|\sqrt{L_0}f + \sqrt{L_{RIS}}h^H X g\right|^2 \rho_S \zeta_T^2 + 1}, \tag{61}$$

respectively.

Given the covariance matric, the statistical parameters (i.e., first and second moments) of the effective channel $\left|\sqrt{L_0}f + \sqrt{L_{RIS}}h^H X g\right|^2$ can be determined. The Gamma distribution approximation of $\left|\sqrt{L_0}f + \sqrt{L_{RIS}}h^H X g\right|^2$ is possible by using the moment-matching method discussed in Section 3. The details on the statistics of

$\left|\sqrt{L_0}f + \sqrt{L_{RIS}}h^H X g\right|^2$ was discussed in the proof of Theorem 1 [49]. Then, by following the similar approach, i.e., using the results of Lemmas 1-4, the tight bounds of the average achievable rate, average residual energy and R-Er tradeoffs using the spatially correlated fading can be derived for the TS and SPS designs.

Now, we show that an i.i.d. channel model can provide a tight (upper) bound of the achievable rate derived in our framework for both SWIPT designs in practical correlated channels. To show the tightness of the bound as in Fig. 2, we show numerical results under the following condition: $\psi_{min} = 1$ (ideal phase-shifting), $M = 100$ (reflecting elements per row = reflecting elements per column = 10), $\lambda = 0.1$m, $\beta = \alpha = 0.6$, $P_C = 3$mW, $\zeta_T = 0.2$, $\rho_S = 80$dB, $P_S = 20$dBm and a correlation matrix is derived as in [48], [49] for correlated fading. The path loss for RIS cascaded channel is calculated by Eq. (1) with the parameters same as in Table 3. The analytical values are calculated by Eqs. (60) and (61) for correlated fading channels and by Eqs. (9) and (10) for i.i.d. fading channels. It can also be observed that the configuration of RIS, i.e., size (side length) of a reflecting element, l, can determine the strength of the spatial correlation and then, it can determine the performance gap between the i.i.d. and correlated channel models. As l increases to $\frac{\lambda}{2}$, the channel correlation is reduced, and the performance of a correlated channel becomes closer to that of an i.i.d. channel. Furthermore, when the strength of a direct channel increases, the effect of the correlated RIS cascaded channel decreases, and then the performance gap between i.i.d. and correlated channels decreases. Since the i.i.d. Rayleigh fading model provides a tight upper bound of the practical correlated fading model, we present the detailed analytical framework and the numerical results with i.i.d. channel model.

Adopting a realistic EH process at the SWIPT receiver, the harvested power increases non-linearly with the input power. The non-linear model in [50], [51] accommodates the saturation effect which arises due to the breakdown region. However, the change in the diode or the rectifier topology may result in different behavior since the saturation effect is circuit-specific. The sigmoid (logistic) function also leads to the analytical intractability of the focused research problem. The proper rectifier design can be helpful to avoid the saturation effect and the detrimental nonlinearity for the input power range of interest [52]. For example, an adaptive rectifier can generate a non-vanishing (consistent) energy conversion efficiency (η) over a range of the operating input power. For the sake of practicality and exact analysis, the non-linear (linear-saturation) model provides the reasonable approximation of the saturation model and generates an increasing (constant) harvesting power in linear (saturation) region [53]. For our analysis, the corresponding residual energy for the TS and SPS operating modes using the non-linear (linear-saturation) EH model can be represented by

$$E_{R_{nl}}^{TS}(\alpha) = \begin{cases} \alpha k_1 W - (1-\alpha)P_C & k_1 W \leq P_{sat.} \\ \alpha P_{sat.} - (1-\alpha)P_C & k_1 W > P_{sat.} \end{cases}, \tag{62}$$
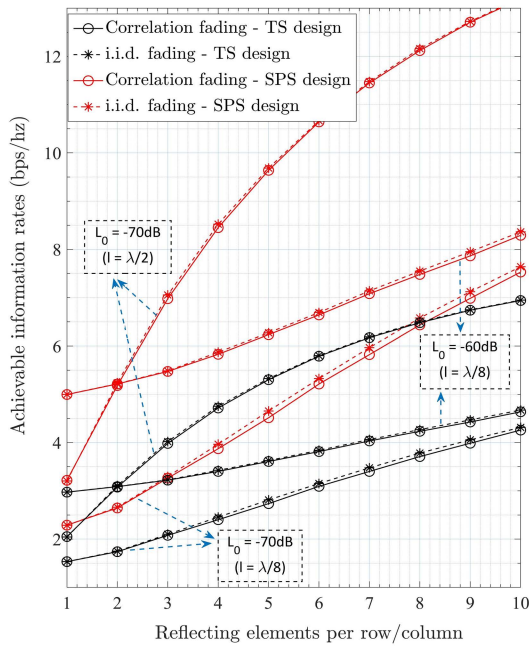
FIGURE 2. Achievable information rates for the TS and SPS designs vs. Number of reflecting elements per row / column.

and

$$E_{R_{nl}}^{SPS}(\beta) = \begin{cases} \beta k_1 W - P_C & k_1 W \le P_{sat.} \\ \beta P_{sat.} - P_C & k_1 W > P_{sat.} \end{cases}, \quad (63)$$

respectively, where $k_1 W$ is the received RF power and $P_{sat.}$ is the saturation threshold (i.e., maximum value of harvested power when the EH process is saturated).

Using Eqs. (62) and (63), the developed analytical framework can be extended for the realistic EH circuits. For the conceptual clarity with the useful insights, we adopt an energy-efficient linear EH model under an assumption that the saturation power is much higher than the operating input power.

V. NUMERICAL RESULTS

In this section, we present the numerical results to validate the derived theoretical expressions and provide valuable insights into the performance of RIS-SWIPT systems. The simulation results are obtained via the Monte Carlo simulations with 10^4 independent trials. The consistency of the numerical and simulation results verify the accuracy of the presented analytical framework. The simulation parameters, if not specified otherwise, are set as in Table 3. Notably, the values are selected for a behavioral validation of the system.

Fig. 3 shows the relationship between the average residual energy for the TS and SPS designs with their respected ratios (i.e., $\overline{E_R^{TS}}$ with α and $\overline{E_R^{SPS}}$ with β). The analytical values are calculated by Eqs. (43) and (52). In detail, the average residual energy for the TS and SPS designs exhibit an incremental relationship with α and β, respectively, as α and β define the time-switching and power-splitting ratios, respectively, for

TABLE 3. Simulation parameters.

Parameter		Value
Total number of reflecting elements	(M)	16
Incident Angle	(θ_i)	$\frac{\pi}{4}$
Rotation Angle	(θ_{Rot})	$\frac{\pi}{8}$
Wavelength of an incident signal	(λ)	0.1 m
Side length of square reflecting element	(l)	$\frac{\lambda}{4}$
Minimum Amplitude	(ψ_{min})	0.4
Practical phase shifter constant	(ϑ)	3
Practical phase shifter constant	(ϖ)	0.4π
RTHI level	(ζ_T)	0.2
Antenna gains at S and D	(G_1, G_2)	5 dB
$S-$RIS and RIS$-D$ distance	(d_1, d_2)	30 m
$S - D$ distance	(d_0)	50 m
Circuit power consumption at D	(P_C)	2 mW
Transmit SNR	(ρ_S)	30 dB

the energy receiver. Furthermore, the TS design outperforms the SPS design. This is due to requirement of keeping the power-consuming information receiver active over an entire transmission-block duration in the SPS design and only over a $(1-\alpha)$ duration in the TS design. The negative impact of P_C on the residual energy performances is also shown. Fig. 4 plots the average achievable information rate for the TS and SPS designs, i.e., $\overline{R_A^{TS}}(\alpha)$ and $\overline{R_A^{SPS}}(\beta)$, respectively, and the transmit SNR (ρ_S). The analytical results are obtained by Eqs. (44) and (53). In detail, the average rate performances increase with ρ_S due to the higher transmission power and $\overline{R_A^{SPS}}(\beta)$ outperforms $\overline{R_A^{TS}}(\alpha)$ which suggests that the SPS design provides the superior rate performance. Further, the damaging effect of RTHIs on the average rate performances is investigated. As expected, RTHIs increase the effective noise level and therefore have a negative effect on the reliability performances. Particularly, the results demonstrate that the impact of ζ_T is more severe (i.e., the reliability performances are more sensitive to RTHIs) at higher ρ_S.

Figs. 3 and 4 also illustrate the impact of amplitude variations (in terms of ψ_{min}) on the average residual energy and average achievable information rate performances, respectively. Instead of increasing ρ_S or a relay link, for the SINR improvement, the deployment of RIS with the phase-alignment for the LoS and RIS cascaded links enhances the rate and residual energy performances. In detail, $\psi_{min} = 1$ corresponds the ideal phase shifting in which ψ_m is set at the maximum value (i.e., 1) regardless of the selected ϕ_m^*. However, $\psi_{min} = 0.4$ corresponds the practical phase shifting in which ψ_m depends on ϕ_m^* and the optimal amplitude adjustment is possible only when ϕ_m^* approaches π or $-\pi$. Otherwise, a setting of ϕ_m^* equal to zero yields the minimum reflection amplitude, i.e., maximizes the power loss of the reflected signal arising due to non-ideal RIS phase-shifting.

Figs. 5-7 plot $\overline{R_A^{TS}}(\overline{E_R^{TS}})$ and $\overline{R_A^{SPS}}(\overline{E_R^{SPS}})$ to show the R-Er tradeoff performances for the TS and SPS designs, respectively, over different values of the physical size and number of the reflecting elements, rotation angle of the RIS plane and reflection amplitude variations. The analytical values are
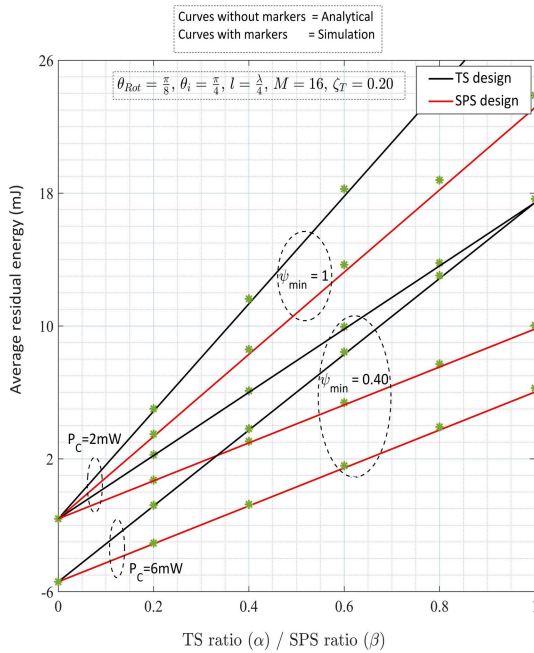
FIGURE 3. Average residual energy for TS design vs. α and average residual energy for SPS design vs. β.

FIGURE 5. R-Er tradeoffs for the TS and SPS designs vs. Size of reflecting elements of the RIS.
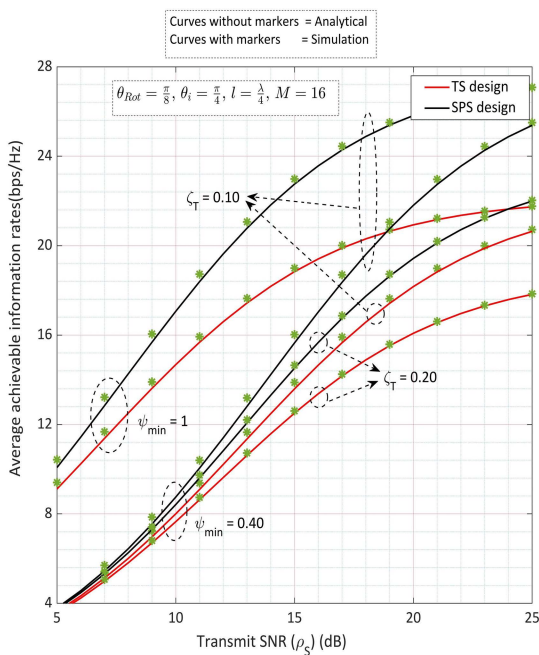

FIGURE 4. Average achievable information rates for the TS and SPS designs vs. Transmit SNR (ρ_S).

calculated by Eqs. (45) and (54). In Figs. 5-7, the average residual energy for both designs is set as 6mJ for an observation point. The results show that $\overline{R_A^{TS}}(\overline{E_R^{TS}})$ is a linear function and $\overline{R_A^{SPS}}(\overline{E_R^{SPS}})$ is a non-linear function. A comparison between the TS and SPS designs also reveals that the SPS design provides the better R-Er tradeoff performance than the TS design. This phenomenon indicates the better
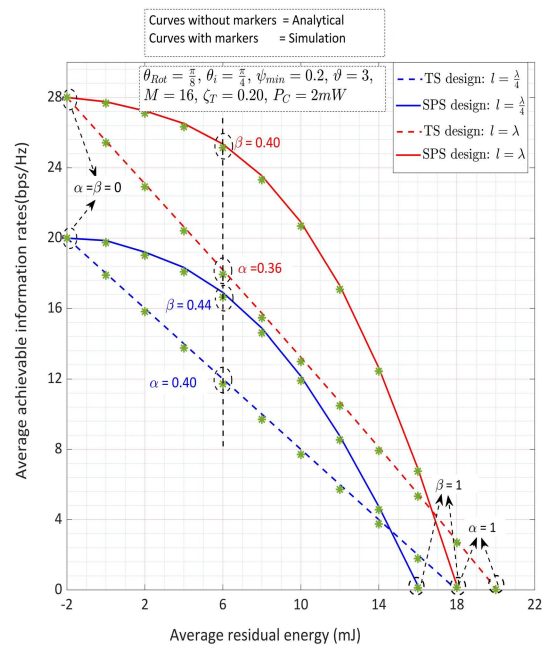
energy-efficient resource allocation for RIS-aided SWIPT systems using the SPS design. Counter-intuitively, the TS design provides the suboptimal performance.

Fig. 5 shows the impact of the side length of the square reflecting element (l) which determines the physical size of the reflecting elements for fixed M. The results suggest that the larger size of the reflecting elements results to the better R-Er tradeoff performance for both designs. The reason is that the area of the RIS becomes larger and consequently the larger passive beamforming gain can be acquired. The counter-intuitive behavior can be shown for fixed $X_R Y_R$ (i.e., the smaller size of the reflecting elements results in the better R-Er tradeoff performances due to increment in the number of reflecting elements). The substantial performance gain with the increment in M or $X_R Y_R$ can be justified by the improved RIS channel power gain. Next, Fig. 6 provides an insight into the placement of the RIS plane and shows the impact of the rotation angle θ_{Rot}. The results show that the smaller $\theta_i - \theta_{Rot}$ causes better R-Er tradeoff performances for the TS and SPS designs since the term $\cos(\theta_i - \theta_{Rot})$ corresponding the effective impinging area of the incident EM wave increases. In detail, larger l and smaller $\theta_i - \theta_{Rot}$ improve the harvested energy and require lesser α (for TS) and β (for SPS) to maintain the target residual energy, and consequently, achieve the improved information rates.

Fig. 7 demonstrates the effect of the phase-dependent amplitude variations and number of reflecting elements. In particular, the non-ideal amplitude response is investigated by varying ψ_{min} and ϑ (i.e., the constants related to the specific circuit implementation of the practical phase shifters). In detail, the optimal system performance setting for the TS
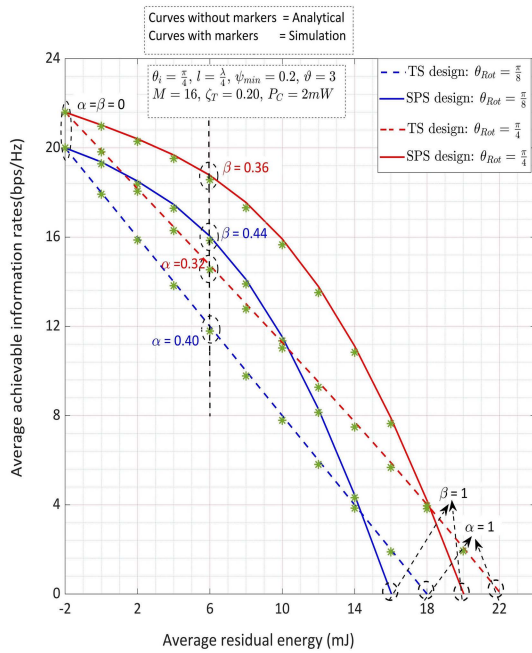
FIGURE 6. R-Er tradeoffs for the TS and SPS designs vs. Rotation angle of the RIS plane.
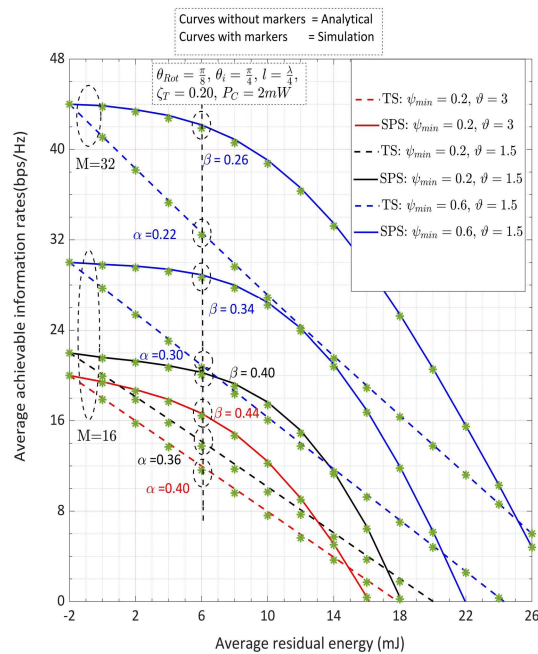

FIGURE 7. R-Er tradeoffs for the TS and SPS designs vs. Constants related to the practical phase shifters.

FIGURE 8. R-Er tradeoffs for the TS and SPS designs vs. Circuit power consumption of *D*.

the large-scale path loss and small-scale Rayleigh fading to improve the system performance.

Fig. 8 shows the impact of circuit power consumption P_C on the R-Er tradeoff performances for the TS and SPS designs, i.e., the achievable information rates are compared for a given residual energy. The SPS design provides the superior performance over the entire range of P_C. As P_C increases, more resources, i.e., time in TS design (α) and power in SPS design (β), are allocated to the energy receiver in order to maintain the target residual energy, and consequently, result in less resource allocation to the information receiver (and less information rates).

VI. CONCLUSION
In this paper, we investigate the RIS-empowered receiver designs for SWIPT systems while adopting various practical issues. We employ the phase-dependent amplitude variations and the additive distortion noise for the non-ideal RIS and transceiver, respectively. Furthermore, the signal model incorporates the area of the RIS and the placement of the RIS plane to phase-align the reflected signals in a direction of interest. The statistical characterization is provided for the tractable performance analysis and the novel analytical tight-bound expressions are derived to quantify the R-Er tradeoffs for the TS and SPS designs. The results demonstrate the selection of the system parameters to provide the design insights and implementation guidelines for RIS-aided SWIPT systems in the 6G era.

and SPS designs is to deviate the ψ_{min} towards unity and ϑ towards zero. Such a setting of ψ_{min} and ϑ requires lesser α and β to maintain the target residual energy and provides the improved information rates. The results also provide the insights of the impact comparison of the ϑ, ψ_{min} and M. It can be observed that the M has the highest impact, followed by ψ_{min}, and then by ϑ. The greatest impact of M can be justify by the fact that the increased number of M influences both
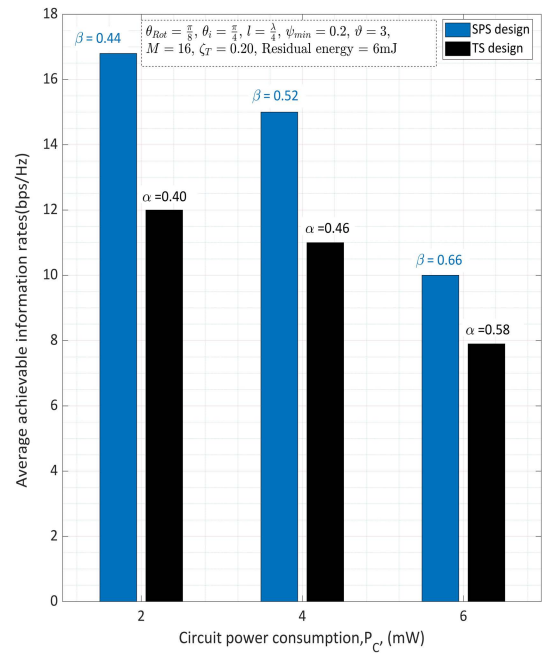
REFERENCES
[1] H. Yu, H. Lee, and H. Jeon, "What is 5G? Emerging 5G mobile services and network requirements," *Sustainability*, vol. 9, no. 10, p. 1848, Oct. 2017.

[2] M. A. Siddiqi, H. Yu, and J. Joung, "5G ultra-reliable low-latency communication implementation challenges and operational issues with IoT devices," *Electronics*, vol. 8, no. 9, p. 981, Sep. 2019.

[3] H. Yu and J. Joung, "Secure IoT communications using HARQ-based beamforming for MISOSE channels," *IEEE Internet Things J.*, vol. 8, no. 23, pp. 17211–17226, Dec. 2021.

[4] W. Khalid and H. Yu, "Security improvement with QoS provisioning using service priority and power allocation for NOMA-IoT networks," *IEEE Access*, vol. 9, pp. 9937–9948, 2021.

[5] R. K. Saha, "Approaches to improve millimeter-wave spectrum utilization using indoor small cells in multi-operator environments toward 6G," *IEEE Access*, vol. 8, pp. 207643–207658, 2020.

[6] M. R. G. Aghdam, B. M. Tazehkand, and R. Abdolee, "On the performance analysis of mmWave MIMO-NOMA transmission scheme," *IEEE Trans. Veh. Technol.*, vol. 69, no. 10, pp. 11491–11500, Oct. 2020.

[7] W. Khalid and H. Yu, "Sum utilization of spectrum with spectrum handoff and imperfect sensing in interweave multi-channel cognitive radio networks," *Sustainability*, vol. 10, no. 6, pp. 1764–1782, May 2018.

[8] W. Khalid and H. Yu, "Optimal sensing performance for cooperative and non-cooperative cognitive radio networks," *Int. J. Distrib. Sensor Netw.*, vol. 13, no. 11, pp. 1–9, Nov. 2017.

[9] W. Saad, M. Bennis, and M. Chen, "A vision of 6G wireless systems: Applications, trends, technologies, and open research problems," *IEEE Netw.*, vol. 34, no. 3, pp. 134–142, Oct. 2020.

[10] S. Noh, J. Lee, H. Yu, and J. Song, "Design of channel estimation for hybrid beamforming millimeter-wave systems in the presence of beam squint," *IEEE Syst. J.*, early access, Jun. 8, 2021, doi: 10.1109/JSYST.2021.3079924.

[11] N.-T. Nguyen, H.-N. Nguyen, N.-L. Nguyen, A.-T. Le, D.-T. Do, and M. Voznak, "Enhancing spectrum efficiency for multiple users in hybrid satellite-terrestrial networks," *IEEE Access*, vol. 9, pp. 50291–50300, 2021.

[12] H. B. Chikha, A. Almadhor, and W. Khalid, "Machine learning for 5G MIMO modulation detection," *Sensors*, vol. 21, no. 5, pp. 1–15, Feb. 2021.

[13] W. Hao, G. Sun, M. Zeng, Z. Chu, Z. Zhu, O. A. Dobre, and P. Xiao, "Robust design for intelligent reflecting surface-assisted MIMO-OFDMA terahertz IoT networks," *IEEE Internet Things J.*, vol. 8, no. 16, pp. 13052–13064, Aug. 2021.

[14] A.-T. Le, N.-D.-X. Ha, D.-T. Do, S. Yadav, and B. M. Lee, "Enabling NOMA in overlay spectrum sharing in hybrid satellite-terrestrial systems," *IEEE Access*, vol. 9, pp. 56616–56629, 2021.

[15] L. Yang, F. Meng, J. Zhang, M. O. Hasna, and M. D. Renzo, "On the performance of RIS-assisted dual-hop UAV communication systems," *IEEE Trans. Veh. Technol.*, vol. 69, no. 9, pp. 10385–10390, Sep. 2020.

[16] D.-T. Do, M.-S. Van Nguyen, M. Voznak, A. Kwasinski, and J. N. de Souza, "Performance analysis of clustering car-following V2X system with wireless power transfer and massive connections," *IEEE Internet Things J.*, early access, Apr. 2, 2021, doi: 10.1109/JIOT.2021.3070744.

[17] L. Yang, F. Meng, M. O. Hasna, and E. Basar, "A novel RIS-assisted modulation scheme," *IEEE Wireless Commun. Lett.*, vol. 10, no. 6, pp. 1359–1363, Jun. 2021.

[18] L. Yang, F. Meng, Q. Wu, D. B. da Costa, and M.-S. Alouini, "Accurate closed-form approximations to channel distributions of RIS-aided wireless systems," *IEEE Wireless Commun. Lett.*, vol. 9, no. 11, pp. 1985–1989, Nov. 2020.

[19] K. W. Choi, S. I. Hwang, A. A. Aziz, H. H. Jang, J. S. Kim, D. S. Kang, and D. I. Kim, "Simultaneous wireless information and power transfer (SWIPT) for Internet of Things: Novel receiver design and experimental validation," *IEEE Internet Things J.*, vol. 7, no. 4, pp. 2996–3012, Apr. 2020.

[20] J.-M. Kang, C.-J. Chun, I.-M. Kim, and D. I. Kim, "Dynamic power splitting for SWIPT with nonlinear energy harvesting in ergodic fading channel," *IEEE Internet Things J.*, vol. 7, no. 6, pp. 5648–5665, Jun. 2020.

[21] T. D. P. Perera, D. N. K. Jayakody, S. K. Sharma, S. Chatzinotas, and J. Li, "Simultaneous wireless information and power transfer (SWIPT): Recent advances and future challenges," *IEEE Commun. Surveys Tuts.*, vol. 20, no. 1, pp. 264–302, 1st Quart., 2018.

[22] L. Yang, J. Yang, W. Xie, M. O. Hasna, T. Tsiftsis, and M. D. Renzo, "Secrecy performance analysis of RIS-aided wireless communication systems," *IEEE Trans. Veh. Technol.*, vol. 69, no. 10, pp. 12296–12300, Oct. 2020.

[23] W. Khalid, H. Yu, R. Ali, and R. Ullah, "Advanced physical-layer technologies for beyond 5G wireless communication networks," *Sensors*, vol. 21, no. 9, pp. 3197–3205, May 2020.

[24] Z. Yang and Y. Zhang, "Optimal SWIPT in RIS-aided MIMO networks," *IEEE Access*, vol. 9, pp. 112552–112560, 2021.

[25] S. Gong, Z. Yang, C. Xing, J. An, and L. Hanzo, "Beamforming optimization for intelligent reflecting surface-aided SWIPT IoT networks relying on discrete phase shifts," *IEEE Internet Things J.*, vol. 8, no. 10, pp. 8585–8602, May 2021.

[26] N. Ashraf, S. A. Sheikh, S. A. Khan, I. Shayea, and M. Jalal, "Simultaneous wireless information and power transfer with cooperative relaying for next-generation wireless networks: A review," *IEEE Access*, vol. 9, pp. 71482–71504, 2021.

[27] W. Cai, H. Li, M. Li, and Q. Liu, "Practical modeling and beamforming for intelligent reflecting surface aided wideband systems," *IEEE Commun. Lett.*, vol. 24, no. 7, pp. 1568–1571, Jul. 2020.

[28] J. Joung, H. Yu, and J. Zhao, "Bandwidth design for energy-efficient unmanned aerial vehicle using space–time line code," *IEEE Syst. J.*, vol. 15, no. 2, pp. 3154–3157, Jun. 2021.

[29] T. Van Chien, L. T. Tu, S. Chatzinotas, and B. Ottersten, "Coverage probability and ergodic capacity of intelligent reflecting surface-enhanced communication systems," *IEEE Commun. Lett.*, vol. 25, no. 1, pp. 69–73, Jan. 2021.

[30] G. Zhou, C. Pan, H. Ren, K. Wang, and Z. Peng, "Secure wireless communication in RIS-aided MISO system with hardware impairments," *IEEE Wireless Commun. Lett.*, vol. 10, no. 6, pp. 1309–1313, Jun. 2021.

[31] C. Cai, X. Yuan, W. Yan, Z. Huang, Y.-C. Liang, and W. Zhang, "Hierarchical passive beamforming for reconfigurable intelligent surface aided communications," *IEEE Wireless Commun. Lett.*, vol. 10, no. 9, pp. 1909–1913, Sep. 2021.

[32] Y. Ai, F. A. P. de Figueiredo, L. Kong, M. Cheffena, S. Chatzinotas, and B. Ottersten, "Secure vehicular communications through reconfigurable intelligent surfaces," *IEEE Trans. Veh. Technol.*, vol. 70, no. 7, pp. 7272–7276, Jul. 2021.

[33] S. Atapattu, T. A. Tsiftsis, R. Fan, P. Dharmawansa, G. Wang, and J. Evans, "Reconfigurable intelligent surface assisted two–way communications: Performance analysis and optimization," *IEEE Trans. Commun.*, vol. 68, no. 10, pp. 6552–6567, Oct. 2020.

[34] C. Hu, L. Dai, S. Han, and X. Wang, "Two-timescale channel estimation for reconfigurable intelligent surface aided wireless communications," *IEEE Trans. Commun.*, vol. 69, no. 11, pp. 7736–7747, Nov. 2021.

[35] W. Khalid, H. Yu, and S. Noh, "Residual energy analysis in cognitive radios with energy harvesting UAV under reliability and secrecy constraints," *Sensors*, vol. 20, no. 10, pp. 2998–3017, May 2020.

[36] H. Yu and J. Joung, "Design of the power and dimension of artificial noise for secure communication systems," *IEEE Trans. Commun.*, vol. 69, no. 6, pp. 4001–4010, Jun. 2021.

[37] T. J. Cui, S. Liu, and L. Zhang, "Information metamaterials and metasurfaces," *J. Mater. Chem. C*, vol. 5, pp. 3664–3668, Mar. 2017.

[38] S. Abeywickrama, R. Zhang, Q. Wu, and C. Yuen, "Intelligent reflecting surface: Practical phase shift model and beamforming optimization," *IEEE Trans. Commun.*, vol. 68, no. 9, pp. 5849–5863, Sep. 2020.

[39] W. Khalid and H. Yu, "Spatial–temporal sensing and utilization in full duplex spectrum-heterogeneous cognitive radio networks for the Internet of Things," *Sensors*, vol. 19, no. 6, pp. 1441–1459, Mar. 2019.

[40] P. Xu, G. Chen, G. Pan, and M. D. Renzo, "Ergodic secrecy rate of RIS-assisted communication systems in the presence of discrete phase shifts and multiple eavesdroppers," *IEEE Wireless Commun. Lett.*, vol. 10, no. 3, pp. 629–633, Mar. 2021.

[41] G. Li, D. Mishra, Y. Hu, and S. Atapattu, "Optimal designs for relay-assisted NOMA networks with hybrid SWIPT scheme," *IEEE Trans. Commun.*, vol. 68, no. 6, pp. 3588–3601, Jun. 2020.

[42] I. S. Gradshteyn and I. M. Ryzhik, *Table of Integrals, Series, and Products*, 7th ed. Amsterdam, The Netherlands: Elsevier, 2007.

[43] W. Khalid, H. Yu, D.-T. Do, Z. Kaleem, and S. Noh, "RIS-aided physical layer security with full-duplex jamming in underlay D2D networks," *IEEE Access*, vol. 9, pp. 99667–99679, 2021.

[44] R. C. E. Johnson and N. L. Johnson, "Method of statistical differentials," in *Survival Models and Data Analysis*. Hoboken, NJ, USA: Wiley, 1999, pp. 69–72.

[45] A. Stuart and J. K. Ord, *Kendall's Advanced Theory of Statistics: Distribution Theory*, vol. 1, 6th ed. London, U.K.: E. Arnold, 1994, pp. 1–676.

[46] S. Kim, J. Y. Lee, and D. K. Sung, "A shifted gamma distribution model for long-range dependent internet traffic," *IEEE Commun. Lett.*, vol. 7, no. 3, pp. 124–126, Mar. 2003.

[47] F. Govaers and H. Alqaderi, "A gamma filter for positive parameter estimation," in *Proc. IEEE Int. Conf. Multisensor Fusion Integr. Intell. Syst. (MFI)*, Karlsruhe, Germany, Sep. 2020, pp. 40–45.

[48] E. Björnson and L. Sanguinetti, "Rayleigh fading modeling and channel hardening for reconfigurable intelligent surfaces," *IEEE Wireless Commun. Lett.*, vol. 10, no. 4, pp. 830–834, Apr. 2021.

[49] T. Van Chien, A. K. Papazafeiropoulos, L. T. Tu, R. Chopra, S. Chatzinotas, and B. Ottersten, "Outage probability analysis of IRS-assisted systems under spatially correlated channels," *IEEE Wireless Commun. Lett.*, vol. 10, no. 8, pp. 1815–1819, Aug. 2021.

[50] E. Boshkovska, D. W. K. Ng, N. Zlatanov, and R. Schober, "Practical non-linear energy harvesting model and resource allocation for SWIPT systems," *IEEE Commun. Lett.*, vol. 19, no. 12, pp. 2082–2085, Dec. 2015.

[51] E. Boshkovska, D. W. K. Ng, N. Zlatanov, A. Koelpin, and R. Schober, "Robust resource allocation for MIMO wireless powered communication networks based on a non-linear EH model," *IEEE Trans. Commun.*, vol. 65, no. 5, pp. 1984–1999, May 2017.

[52] B. Clerckx, R. Zhang, R. Schober, D. W. K. Ng, D. I. Kim, and H. V. Poor, "Fundamentals of wireless information and power transfer: From RF energy harvester models to signal and system designs," *IEEE J. Sel. Areas Commun.*, vol. 37, no. 1, pp. 4–33, Jan. 2019.

[53] J.-M. Kang, I.-M. Kim, and D. I. Kim, "Joint Tx power allocation and Rx power splitting for SWIPT system with multiple nonlinear energy harvesting circuits," *IEEE Wireless Commun. Lett.*, vol. 8, no. 1, pp. 53–56, Feb. 2019.

WAQAS KHALID received the B.S. degree in electronics engineering from the GIK Institute of Engineering Sciences and Technology, Khyber Pakhtunkhwa, Pakistan, in 2011, the M.S. degree in information and communication engineering from Inha University, Incheon, South Korea, in 2016, and the Ph.D. degree in information and communication engineering from Yeungnam University, Gyeongsan, South Korea, in 2019. He is currently a Research Professor with the Institute of Industrial Technology, Korea University, Sejong, South Korea. His research interests include physical layer modeling, signal processing for wireless communications, and emerging solutions and technologies for 5G/6G networks, such as reconfigurable intelligent surfaces, energy harvesting, physical layer security, NOMA, cognitive radio, UAVs, and the IoTs.

HEEJUNG YU (Senior Member, IEEE) received the B.S. degree in radio science and engineering from Korea University, Seoul, South Korea, in 1999, and the M.S. and Ph.D. degrees in electrical engineering from the Korea Advanced Institute of Science and Technology (KAIST), Daejeon, South Korea, in 2001 and 2011, respectively. From 2001 to 2012, he was with the Electronics and Telecommunications Research Institute (ETRI), Daejeon. From 2012 to 2019, he was with Yeungman University, South Korea. He is currently a Professor with the Department of Electronics and Information Engineering, Korea University, Sejong, South Korea. His research interests include statistical signal processing and communication theory.

JUPHIL CHO received the Ph.D. degree in electronics engineering from Chonbuk National University, in 2001. From 2000 to 2005, he was a Senior Researcher with ETRI, Daejeon, South Korea, where he was involved in the development of the 4G cellular system. He worked as an Invited Researcher with ETRI, in 2006, and stayed as an Invited Professor with the University of South Florida (USF), in 2011 and 2012. Since 2005, he has been a Professor with the Department of Integrated IT & Communication Engineering, Kunsan National University, Kunsan, South Korea. His current research interests include the wireless communication technology, including spectrum sensing, 5G, LED-ID communication, and AI smart housing.

ZEESHAN KALEEM (Senior Member, IEEE) received the B.S. degree in electrical engineering from the University of Engineering and Technology (UET), Peshawar, in 2007, the M.S. degree in electronics engineering from Hanyang University, South Korea, in 2010, and the Ph.D. degree in electronics engineering from Inha University, South Korea, in 2016. He is currently an Assistant Professor with the Electrical and Computer Engineering Department, COMSATS University Islamabad, Wah Campus. His current research interests include public safety networks, 5G system testing and development, and unmanned air vehicle (UAV) communications. He consecutively received the National Research Productivity Award (RPA) awards from the Pakistan Council of Science and Technology (PSCT), from 2016 to 2017, and from 2017 to 2018. He won the only Higher Education Commission (HEC) Best Innovator Award, in 2017. He has published over 60 technical journal articles, book chapters, and conference papers in reputable journals/venues, and has 21 U.S. and Korean registered patents. He was a co-recipient of the Best Research Proposal Award from SK Telecom, South Korea. He is also serving as an Associate Technical Editor for prestigious journals/magazines, such as the IEEE TRANSACTIONS ON VEHICULAR TECHNOLOGY, IEEE OPEN JOURNAL OF THE COMMUNICATIONS SOCIETY (OJ-COMS), *Computer and Electrical Engineering* (Elsevier), *Human-Centric Computing and Information Sciences* (Springer), and the *Journal of Information Processing Systems*. He is also the Guest Editor for special issues of IEEE WIRELESS COMMUNICATIONS, *IEEE Communications Magazine*, IEEE ACCESS, *Sensors*, IEEE/KICS JOURNAL OF COMMUNICATIONS AND NETWORKS, and *Physical Communications*. He has served as a TPC member for world-distinguished conferences, such as the IEEE Globecom, IEEE VTC, IEEE ICC, and IEEE PIMRC.

SHABIR AHMAD (Member, IEEE) received the B.S. degree in computer system engineering from the University of Engineering and Technology, Peshawar, Pakistan, the M.S. degree in computer software engineering from the National University of Science and Technology, Islamabad, Pakistan, in 2013, and the Ph.D. degree from the Department of Computer Engineering, Jeju National University, Republic of Korea. He is currently working as a Research Professor with the Department of IT Convergence Engineering, Gachon University, South Korea. His research interests include the Internet of Things application, cyber-physical systems, and intelligent systems.

● ● ●